Rupture process of the 2011 off the Pacific coast of Tohoku Earthquake (M_w 9.0) as imaged with back-projection of teleseismic *P*-waves

Dun Wang[1,2] and Jim Mori[1]

[1]*Disaster Prevention Research Institute, Kyoto University, Kyoto, Japan*
[2]*Institute of Seismology, China Earthquake Administration, China*

We use the back-projection method, with data recorded on the dense USArray network, to estimate the rupture propagation for the M_w 9.0 earthquake that occurred offshore of the Tohoku region, Japan. The results show a variable rupture propagation ranging from about 1.0 to 3.0 km/s for the high-frequency radiation. The rupture propagates over about 450 km in approximately 150 s. Based on the rupture speed and direction, the high-frequency source process can be divided into two parts. The first part has a relatively slow rupture speed of 1.0 to 1.5 km/s and propagates northwestward. In the second part, the rupture progresses southwestward starting with a slow speed of about 1.5 km/s and accelerating to about 3.0 km/s. We see three large pulses at 30 s, 80 s and 130 s. The first two, including the largest second pulse, were located 50 to 70 km northwest of the epicenter. The third occurred about 250 km southwest of the epicenter. The variability of rupture velocity may be associated with significant changes of physical properties along the fault plane. Areas of low/high rupture speed are associated with large/small energy releases on the fault plane. These variations may reflect the strength properties along the fault. Also, locations of the high-frequency radiation derived from the back-projection analysis are significantly different from the areas of very large slip for this earthquake.
Key words: Back-projection, the 2011 Tohoku Earthquake, high frequency energy, rupture velocity.

1. Introduction

The great 2011 off the Pacific coast of Tohoku Earthquake (M_w 9.0) on March 11, 2011 at 05:46 (UTC) occurred offshore of the east coast of Honshu, Japan and caused a devastating tsunami with considerable loss of life and property. The sequence started with a *M* 7.2 earthquake east of Miyagi Prefecture on March 9 at 02:45 (UTC). The mainshock followed two days later with the hypocenter about 40 km southwest of the previous event. There have been many aftershocks, including three events greater than *M* 7. In order to investigate the rupture propagation and energy release of this earthquake, we used a back-projection technique with the USArray data. As shown by Ishii *et al.* (2005), the back-projection can image the rupture extent, duration and speed of large earthquakes. Past studies have estimated the rupture velocities of the Denali and Kokoxili earthquakes (Walker and Shearer, 2009) and 2008 Wenchuan, China earthquake (Xu *et al.*, 2009; Mori and Smyth, 2009; Zhang and Ge, 2010). For large earthquakes, rupture velocity is an important parameter that reflects the fault properties and rupture complexity. For example, tsunami earthquakes usually have slow rupture velocities due to rupture complexity and/or low rigidity material, whereas some onshore crustal earthquakes can have very fast supershear speeds that might be attributed to the accumulated stress and smoothness of the fault planes.

2. Data and Method

The back-projection method has been used recently to study the rupture process of a number of large and moderate earthquakes (e.g. Ishii *et al.*, 2005; Mori *et al.*, 2009; D'Amico *et al.*, 2010). Our analyses use broadband vertical components from USArray stations, which are located mainly in the southwest and central regions of the United States. Of 693 available stations, we chose data from 412 sites that had generally similar waveforms by evaluating the cross-correlations of the beginning 6 seconds of the *P* waves for each station. This procedure eliminates data that have strong site response or possible instrumental problems. The array is located at distances of 65 to 96 degrees from the earthquake and clearly records the *P* wave. The farther stations are in the *P*-diffracted range, however, the waveforms still look very similar to the data recorded at closer distances (see Fig. 1), and therefore it seems acceptable to include these data. We used the unfiltered velocity data and also data high-pass filtered at 0.5 Hz and 1.0 Hz. For the back-projection calculation, we set a grid of 61 × 16 points (600 × 176 km^2) in the source area which covers most of the aftershock region. The northwest corner is located at 40.7502°N, 141.9144°E and the southeast corner at 35.1498°N, 141.9333°E. The trend of the grid is oriented 15° east of north. Our back-projection analysis does not have very good depth resolution, so that the assumed depths of the grid points do not significantly affect the results. We used a constant depth of 20 km for calculating the
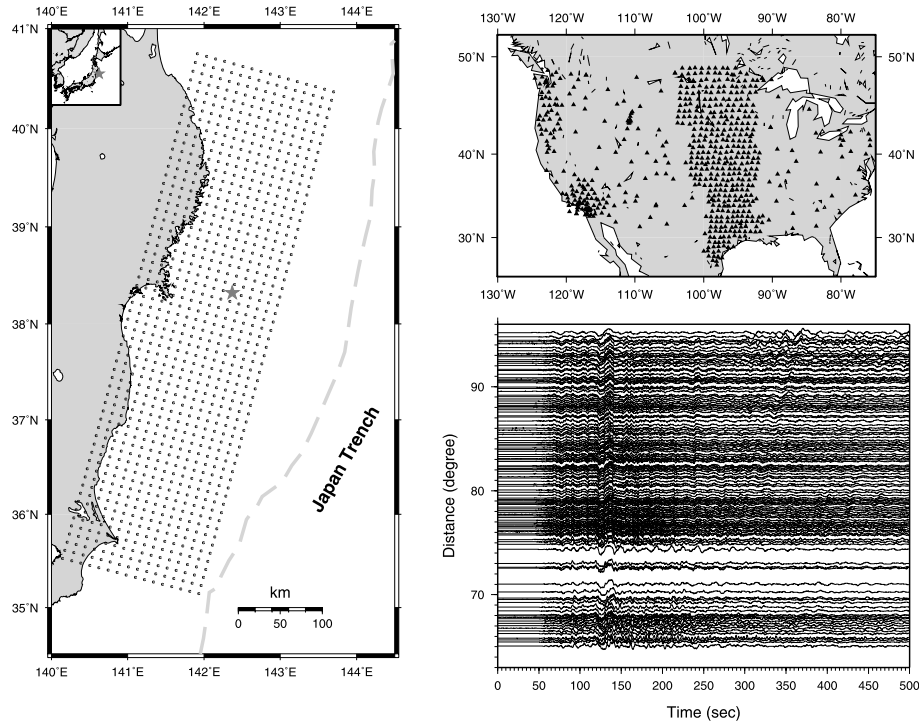
Fig. 1. Grid of source locations tested for each time window (left), location of the stations (top right), seismograms used for the analyses (bottom right). The first arrivals at time 50 s are aligned using a waveform cross-correlation.

travel times. We also tried a wider grid that extends to, and past, the trench to the east, but the results in this study show that the determined source locations are all west of the epi-center. The back-projection method determines which grid points are the sources of seismic radiation in each desig-nated time window of the *P* wave. This is done by first aligning all waveforms on the first arrival using waveform cross-correlations (Fig. 1) and the initial source location is constrained to the epicenter (38.322°N, 142.369°E, as de-termined by the USGS). Since we are using teleseismic data we use the USGS location which should correspond to the teleseismic first arrivals. This procedure corrects for any static station corrections in the travel times to each site. Then, for each subsequent time window (j_{tim}), sums of the squared amplitude stacks of the waveforms, $S(j_{\text{grid}}, j_{\text{tim}})$, are calculated, assuming a source at each grid point (j_{grid}), with the following equation.

$$S\left(j_{\text{grid}}, j_{\text{tim}}\right) = \sum_{i_{\text{pt}}} \left[\sum_{i_{\text{sta}}} \left(s(i_{\text{sta}}, i_{\text{pt}} - to_{i_{\text{sta}}}) \right) \right]^2 \quad (1)$$

where $s(i_{\text{sta}}, i_{\text{pt}} - to_{i_{\text{sta}}})$ are time series for each station, i_{sta}. Time shifts, $to_{i_{\text{sta}}}$, for each station in the stack were calculated using the theoretical travel times from the sta-tion to the grid point, using the software TauP (Crotwell *et al.*, 1999) and the velocity structure IASPEI 1991 (Kennett, 1991). For each time window, j_{tim}, the stack amplitude for each grid point, j_{grid}, is calculated using the time series of points, i_{pt}, running from 10 s before, to 10 s after, the the-oretical travel time. These stack amplitudes are compared and the points that show the largest stack amplitudes are in-terpreted to be the locations of the radiation. From the onset of the *P* wave, we used 20 s time windows that are offset

by 2 s. Eighty overlapping windows were used for a total duration of 160 s.

3.　Results

The snapshots in Fig. 2 show the locations associated with the waveform stacks that have the highest amplitude for each time window, and therefore are inferred to be the dominant source of the *P*-wave radiation. The colors in the snapshots show the stack amplitudes (calculated with Eq. (1)) for each time window, normalized by the largest overall amplitude, to reflect the relative distribution of radi-ated energy release. The results for 20 s time windows of the 1.0 Hz high-pass filtered data show the rupture propaga-tion for the earthquake most clearly. The rupture first moves toward the northwest with a rather slow speed . The first large pulse 30 s after the origin time is located about 40 km northwest of the epicenter. Then, the largest pulse occurs at about 70 s and 90 km west-northwest of the epicenter. From this time, the rupture appears to change direction and begins to move toward the southwest. At first, the rupture speed is rather slow at about 1.5 km/s then from 100 to 150 s it accelerates and progresses toward the southwest at a faster speed. These results can best be seen in the anima-tion of the 2 s time windows at http://www.eqh.dpri.kyoto-u.ac.jp/˜mori/Sendai/sendai.htm.

The top portion of Fig. 2 shows the time series of the (squared) stack amplitudes for each time window, as cal-culated by Eq. (1). The unfiltered data (gray line) shows one large pulse which is located northwest of the epicenter. The 1 Hz high-pass data (black line) and similar 0.5 Hz high-pass data (yellow line), show three large subevents, with the two larger ones occurring in the general region of the epicenter. The longer period results may be representa-
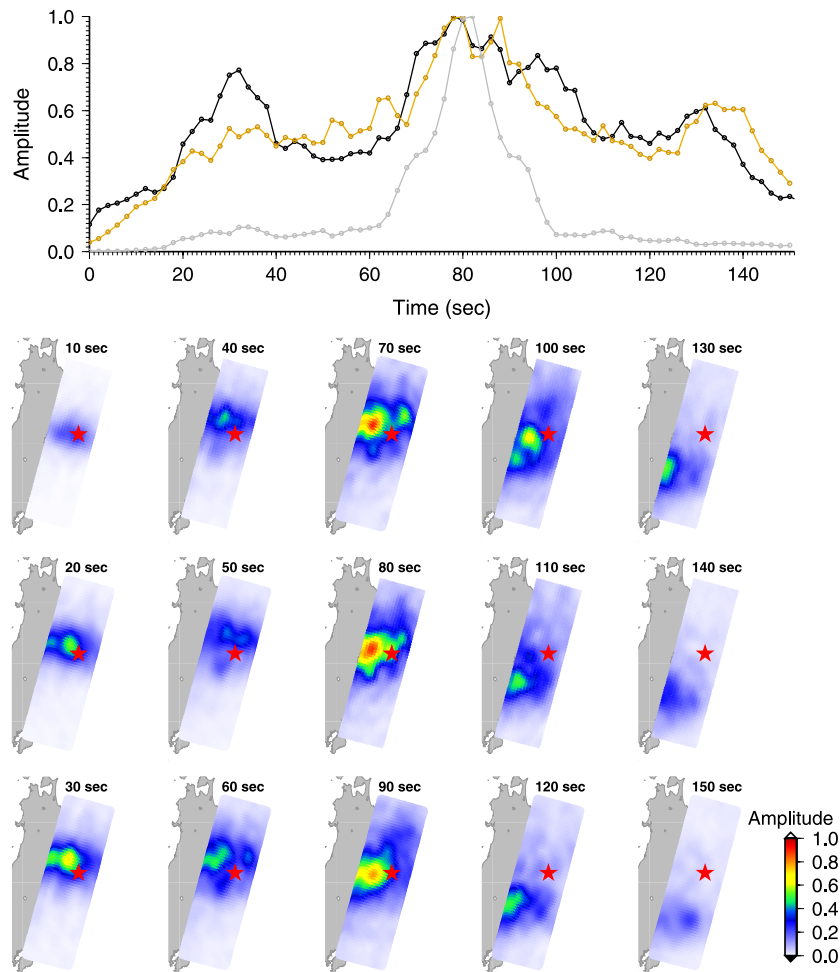
Fig. 2. Top shows the normalized values of the maximum amplitudes (sums of squared amplitude stacks) in each time window for the unfiltered data (gray line), 0.5 Hz high-pass (yellow line) and 1.0 Hz high-pass (black line). Bottom shows snap shots of the rupture propagation in 10 s windows for the 1.0 Hz high-pass data. Colors show values of the squared amplitude stacks at each grid point. The initial arrivals were constrained to originate from the epicenter marked by the red star.

tive of the continuous slip which seems to be dominated by one area of large slip. However, even these unfiltered data probably do not contain sufficient long-period information to correctly map out the total slip distribution. The filter ranges were chosen to look at a range of frequencies with constraints of the data and method. The higher frequencies around 3 Hz are much less coherent so the rupture cannot be seen clearly, and the lower frequencies around 0.1 Hz lose spatial resolution for imaging the details of the rupture.

To estimate the speed of propagation of the rupture, Fig. 3 plots the positions and times of the maximum stack amplitude for each time window at 2 s intervals, using the 1.0 Hz high-pass filtered data. We can see a change of the direction of the rupture propagation at about 70 s, so for estimating the rupture speed we separate the fault area into two regions. For the first 70 s, we use the epicenter as the reference point, and we obtain rupture velocities of 1.0 to 1.5 km/s (upper right portion of Fig. 3). For the points after 70 s, we use the location of the large stack amplitude in the 70 s window as the reference point, and obtain values of about 1.5 to 3.0 km/s for the second part of the rupture (lower right portion of Fig. 3).

4. Discussion

Our results show a significantly variable speed for the rupture propagation of this huge earthquake. The rupture velocity for the first part of the earthquake source is relatively slow at 1.0 to 1.5 km/s and for the second part the values accelerate from about 1.5 km/s to about 3.0 km/s. The rupture speed can be linked with physical properties on the fault surface, and may show the relative amount of non-radiated energy, such as fracture energy (Fossum and Freund, 1975; Kanamori and Brodsky, 2004). Higher fracture energy implies processes with more dissipated (non-radiated) energy and may be an indication of lower dynamic friction (Kanamori and Brodsky, 2004), For this earthquake, the areas of slow rupture speed seem to be associated with the areas of large slip near the hypocenter. In contrast, the areas of higher rupture velocity and less slip can correspond to lower fracture energy, indicating more brittle failure on a high friction fault. Thus, the spatial distribution of rupture speed determined in this study (Fig. 3) may be interpreted in terms of differences in dynamic friction on the fault. Although there are many complicating factors that control the fracture energy and rupture velocity (Bizzari, 2010) that need to be clarified to support this interpretation.
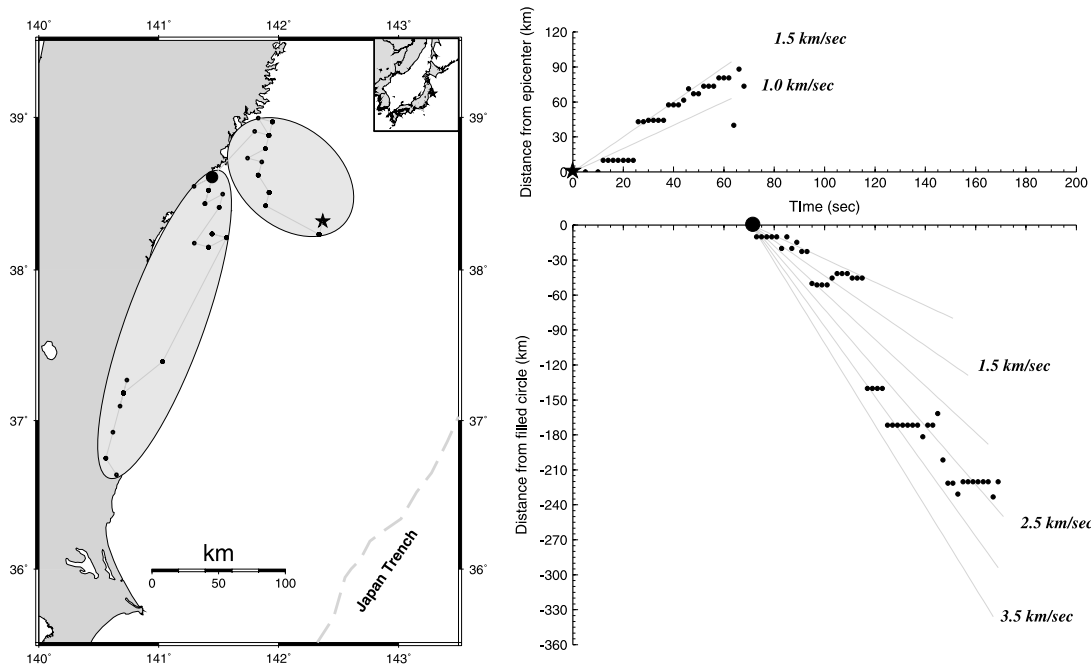
Fig. 3. Left: Locations of the points associated with the maximum stack amplitude in each time window. Right: Distance as a function of time for the location of the maximum stack amplitude in each time window, as measured from the epicenter (star) for the first portion of the rupture and from the location of the filled circle for the second portion of the rupture. Straight lines show the rupture velocities for reference.
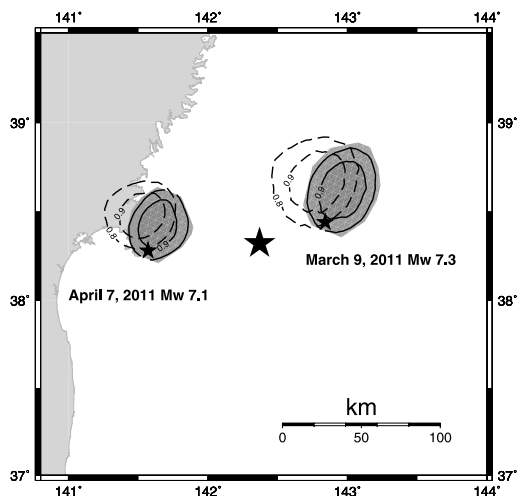

Fig. 4. Back-projection results showing the locations of the centroids of the total radiated energy for two test events. Shaded gray areas are squared stack amplitudes for the March 9 foreshock (right) and April 7 aftershock (left), using static corrections derived from cross-correlations of the respective onsets. Dashed contour lines show the same, except that static corrections derived from the mainshock (large star) onset were used. Contour lines show 80 percent and 90 percent of the maximum.

One interesting aspect of our results is that the (high frequency) rupture track we show in Fig. 3 is along the deeper down-dip edge of the aftershock zone. This is very different from the areas of large slip for this earthquake, as inferred from geodetic, tsunami, and teleseismic slip models. To further examine this result, we carried out the same analyses on several other events within the aftershock area, to check if there is any systematic east-west bias in our results. Figure 4 shows the total radiated energy of the

back projection results for two large events on March 9, 2011 (M_w 7.3) and April 7, 2011 (M_w 7.1). The March 9 event is located east of the mainshock epicenter at a slightly shallower depth. The April 7 event is located west of the mainshock epicenter at a depth similar to that of the sources we see in our back projection. The back projection is calculated in two ways: 1) The shaded areas show squared stack amplitudes using static corrections derived from cross-correlations of the respective onsets; 2) The dashed contours are the same, except using the static time shifts determined for the mainshock and applied to the two test events. All four results show centroids that are located north of the epicenters (stars), indicating northward propagation for both events. There is a 10 to 15 km east-west shift between the two methods which gives some indication of the location errors for our rupture track of the mainshock. The back projection results from the smaller events increases our confidence that the imaging of the higher frequency radiation for the mainshock is correct. This provides clear evidence that the high-frequency sources are originating from different parts of the fault than the areas of very large slip closer to the trench.

References

Bizzari, A., On the relations between fracture energy and physical observables in dynamic earthquake models, *J. Geophys. Res.*, **115**, B10307, doi:10.1029/2009JB007027, 2010.

Crotwell, H. P., T. J. Owens, and J. Ritsema, The TauP Toolkit: Flexible seismic travel-time and ray-path utilities, *Seismol. Res. Lett.*, **70**, 154–

160, 1999.

D'Amico, S., K. D. Koper, R. B. Herrmann, A. Akinci, and L. Malagnini, Imaging the rupture of the Mw6.3 April 6, 2009 L'Aquila, Italy earthquake using back-projection of teleseismic P-waves, *Geophys. Res. Lett.*, **37**, L03301, doi:10.1029/2009GL042156, 2010.

Fossum, A. E. and L. B. Freund, Nonuniformly moving shear crack model of a shallow focus earthquake mechanism, *J. Geophys. Res.*, **80**, 3343–3347, 1975.

Ishii, M., P. Shearer, H. Houston, and J. E. Vidale, Extent, duration and speed of the 2004 Sumatra-Andaman earthquake imaged by the Hi-Net array, *Nature*, **435**, 933–936, 2005.

Kanamori, H. and E. E. Brodsky, The physics of earthquakes, *Rep. Prog. Phys.*, **67**, 1429–1496, 2004.

Kennett, B. L. N., *IASPEI 1991 Seismological Tables*, edited by Kennett, B. L. N., 167 pp, Canberra: Research School of Earth Sciences, Australian National University, 1991.

Mori, J. and C. Smyth, A summary of seismological observations for the May12, 2008 Wenchuan, China earthquake, in *Investigation Report of the May 12th 2008 Wenchuan Earthquake, China*, http://shake.iis.u-tokyo.ac.jp/wenchuan/, 2009.

Walker, K. T. and P. M. Shearer, Illuminating the near-sonic rupture velocities of the intracontinental Kokoxili Mw 7.8 and Denali fault Mw 7.9 strike-slip earthquakes with global P wave back projection imaging, *J. Geophys. Res.*, **114**, B02304, doi:10.1029/2008JB005738, 2009.

Xu, Y., K. D. Koper, O. Sufri, L. Zhu, and A. R. Hutko, Rupture imaging of the Mw 7.9 12 May 2008 Wenchuan earthquake from back projection of teleseismic P waves, *Geochem. Geophys. Geosyst.*, **10**, Q04006, doi:10.1029/2008GC002335, 2009.

Zhang, H. and Z. Ge, Tracking the rupture of the 2008 Wenchuan Earthquake by using the relative back-projection method, *Bull. Seismol. Soc. Am.*, **100**, 2551–2560, 2010.

D. Wang (e-mail: dunwang@eqh.dpri.kyoto-u.ac.jp) and J. Mori